

See discussions, stats, and author profiles for this publication at: <https://www.researchgate.net/publication/288854793>

Axial Movement Parameter Study on Preclinical Slit-Slat SPECT

Article in IEEE Transactions on Nuclear Science · December 2015

DOI: 10.1109/TNS.2015.2493043

CITATIONS

0

READS

89

3 authors, including:



Tianyu Ma

Tsinghua University

125 PUBLICATIONS 346 CITATIONS

[SEE PROFILE](#)



Rutao Yao

University at Buffalo, The State University of New York

66 PUBLICATIONS 730 CITATIONS

[SEE PROFILE](#)

Some of the authors of this publication are also working on these related projects:



PET based PET/SPECT Dual Modality System [View project](#)

Axial Movement Parameter Study on Preclinical Slit-Slat SPECT

Sida Wang, Tianyu Ma, *Member, IEEE*, and Rutao Yao, *Senior Member, IEEE*

Abstract—One challenge to discrete detector slit-slat SPECT is that the system's resolution and sensitivity vary significantly in the axial direction. The objective of this work was to reduce the variation by introducing axial movement and to determine the corresponding parameters, i.e. step size (D) and total length (L). We calculated the system response matrix of the slit-slat SPECT system and evaluated the system's axial-direction resolution and sensitivity as functions of axial positions in the field of view. A series of scan protocols with combined rotational and axial movements, that is, helical scans, were applied to simulated phantom studies to select the preferred L and D values. Introducing axial movement effectively improved the system's axial-direction sensitivity uniformity and reconstructed image resolution in both axial direction and in transverse plane, and it also reduced the artifacts in the transverse plane. The preferred choice of L is the cycle of the periodic pattern formed by the slit collimator's and detector crystals. As about the value of D , a smaller D value is preferred for better uniformity as well as resolution improvement but practical constraints would apply.

Index Terms—Helical scan, slit-slat collimator, SPECT.

I. INTRODUCTION

SMALL animal single photon emission computed tomography (SPECT) is an essential tool for preclinical biomedical research. To expand the availability of SPECT, we developed SPECT imaging capability on an existing animal PET scanner [1] with a slit-slat collimator insert [2]–[5]. Slit-slat collimator consists of a rotatable tube with multiple slits axially grooved on the wall of the tube, and a set of annular-shaped septa stacked in the axial direction. Its main benefit as compared to a multiple pinhole collimator is the large field-of-view (FOV) which is advantages for whole body animal imaging.

We learned from a previous study [6] the slit-slat add-on SPECT suffers significant system response variation in the axial direction, which leads to non-uniformity of imaging quality. This is caused by the photon transportation process through two discrete response functions, formed by the discrete slit collimator geometry and the discrete PET detector crystals. The solution of this problem, however, has not been reported in the literature.

Manuscript received April 13, 2015; revised August 06, 2015; accepted October 16, 2015. Date of publication December 29, 2015; date of current version February 16, 2016.

S. Wang and T. Ma are with the Department of Engineering Physics, Tsinghua University, Beijing 100084, China.

R. Yao is with the Department of Nuclear Medicine, State University of New York at Buffalo, Buffalo, NY 14214 USA (e-mail: rutaoyao@buffalo.edu).

Color versions of one or more of the figures in this paper are available online at <http://ieeexplore.ieee.org>.

Digital Object Identifier 10.1109/TNS.2015.2493043

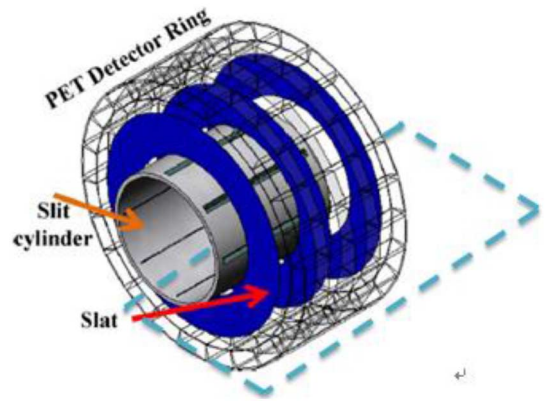


Fig. 1. Diagram of a PET scanner detector ring with a slit-slat collimator insert. This is the setup for performing SPECT imaging on an existing PET scanner. The dashed lines indicate the plane where the axial sectional view is taken in Fig. 2.

The objective of this work was to evaluate the effect of adding axial movement to the rotational tomographic projection acquisition to improve the response uniformity and to identify the most suitable axial sampling parameters. The concept is intuitive but similar studies have not been seen in literature—with axial movement each point in an imaging object is sampled at different axial locations and the point's overall system response is the sum of all axial samples, which shall have an averaging effect to reduce response non-uniformity.

II. MATERIALS AND METHODS

A. Animal PET Scanner

The simulation studies performed in this work were based on a LabPET-8 scanner [7]. The scanner consists of 32 crystal rings - LGSO and LYSO interleaved crystal rings. Each ring consists of 192 crystals. Each crystal is $2 \times 2 \times 14(\text{LGSO})/12(\text{LYSO}) \text{ mm}^3$ in size. The inner diameter of the detector ring is 162 mm, and axial coverage of the detector is 75.2 mm.

B. Slit-slat Collimator Insert

Fig. 1 shows the diagram of the LabPET-8 detector ring with a slit-slat collimator placed within. The collimator consists of a rotatable tungsten tube grooved with 6 slits, and a stack of annular shaped thin tungsten plates (slats) interleaved with hard foam spacers. The spacers were replaced with air in all simulations in this work. Six slit-apertures with a length of 76 mm

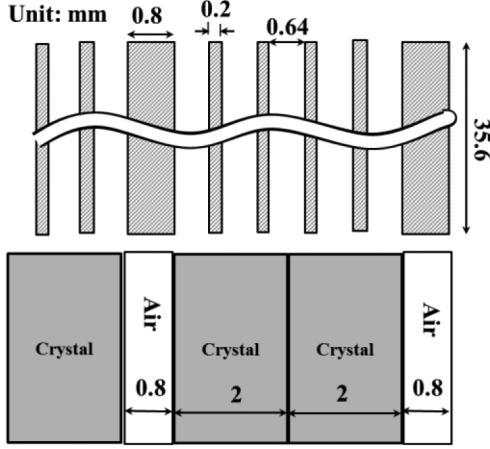


Fig. 2. Diagram illustrating the partial axial sectional view of the slit-slat collimator inserted in the gantry of LabPET-8. The plane where the cross-sectional view is shown is indicated by dashed green rectangle in Fig. 1.

are uniformly distributed on the tube along axial direction. The inner diameter of the tube is 67.8 mm and the wall thickness is 2.5 mm. The opening width and angle of the slit aperture are 1.3 mm and 95° , respectively. The inner and outer diameters of the slats are 76.8 mm and 148 mm respectively. There are 81 slats in total in the collimator assembly. The axial axes of the slat stack, the slit tube and the PET detector ring are all aligned. The expected FOV of the SPECT unit is 50 mm diameter \times 76 mm length.

A partial axial sectional view of the collimator and detector ring is shown in Fig. 2. The location of the section is indicated by the dashed lines in Fig. 1. The intervals between the slats were selected - every 4 thin slats (thickness of 0.20 mm) were interleaved with 5 spacers of 0.64 mm, followed with one thick slat (0.8 mm) - so that the slat configuration cycle matches the cycle of the crystal arrangement in the axial direction.

C. Characteristics of Resolution and Sensitivity along the Axial Direction

We calculated the point spread functions (PSFs) of the system using an analytical approach [8]. Only the geometric efficiency, i.e. the solid angle that allows the lights from point sources to shine through the collimator openings and reach detector crystals, is accounted. This corresponds to, as shown in Fig. 3, the calculation of the crystal area S upon which the light from a point source at location P shed. P is the location of the point source. The detector efficiency was assumed to be 100% because of the high efficiency of PET detectors in stopping 140 keV gamma rays for SPECT imaging.

The 2-D fan beam geometry formed by the slit-slat collimator allows us to assume the system response can be analyzed independently in the axial direction and in the transverse plane [2]. In this study, we focus only on the characteristics of axial response. The following definitions only consider the crystal index m and point source location P in the axial direction Z .

Let the solid detection angle $\Omega_{P,k,m}$ correspond to the area on the m th crystal exposed to the light that originates from point P and passes through the opening k of the slit-slat collimator.

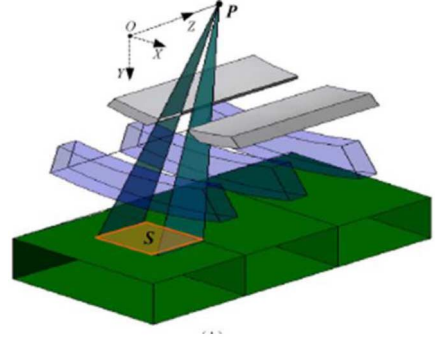


Fig. 3. A PSF for image voxel at P is calculated from the crystal area exposed to light originating from P and passing through a slit-slat collimator opening.

Then, the corresponding PSF - only axial direction variable m is indicated - is [8],

$$f_{P,m} = \sum_k \frac{\Omega_{P,k,m}}{4\pi} \quad (1)$$

We chose root mean square (RMS) width, rather than FWHM, as the resolution index to quantify the spread of PSF. This is because PSFs usually only spread over 2 to 4 crystals, or 2 to 4 sampling points, due to the large pixelated crystal size used [8], [9], and FWHM is not suitable to estimate resolution in this situation.

$$RMS_{P,z} = \sqrt{\frac{\sum_{m=m_0}^{m_0+M-1} f_{P,m} \cdot (z_m - \bar{z}_\lambda)^2}{\sum_{m=m_0}^{m_0+M-1} f_{P,m}}} \quad (2)$$

$$\bar{z}_\lambda = \frac{\sum_{m=m_0}^{m_0+M-1} f_{P,m} z_m}{\sum_{m=m_0}^{m_0+M-1} f_{P,m}},$$

where m_0 is the start crystal index of the $[f_{P,m}]$, z_m is m th crystal's center coordinate in Z direction, M is the number of crystals within PSF's effective range, and \bar{z}_λ is the centroid of $[f_{P,m}]$.

The sensitivity S_P for a point at axial position P is the ratio of the photons detected by all the crystals to the total photons emitted from that point [5]. Explicitly

$$S_P = \sum_{m=1}^M f_{P,m}. \quad (3)$$

The RMS width and sensitivity of a helical scan, RMS_P^h and S_P^h , respectively, correspond to the overall effect of multiple axial samples,

$$RMS_P^h = \frac{\sum_{n=1}^N RMS_{P+nD}}{N}, \quad (4)$$

$$S_P^h = \frac{\sum_{n=1}^N S_{P+nD}}{N}, \quad (5)$$

where n is the step index of axial translational movement, D is the axial step size and N is the total number of steps.

D. Evaluation of Axial Movement Parameters

A SPECT scan now involves two axial movement parameters of the object being imaged: step size D and distance L . We studied 52 scan protocols formed by permutation of 4 D and 13 L values. The 4 D values were 0.2 mm to 0.8 mm, with an increment step size of 0.2 mm. The 13 L values were from 0.0 mm to 4.8 mm, with an increment step size of 0.4 mm.

To focus this study on axial sampling, the angular step size of the slit-tube rotation was fixed at 6° , which was calculated from the estimated spatial resolution at the center of field-of-view (CFOV) [2] and the angular sampling theorem [10]. The total number of rotational steps for completing a 360° tomographic acquisition is 60. The translational and rotational movements were integrated in the way so that the steps of both movements are interleaved to complete desired cycles in both the axial and angular directions. For example, given D is 0.2 mm and L is 0.8 mm, the image object would move 0.2 mm first, then rotate 12 steps with 6° per step and a projection is acquired at each rotational stop. This sequence repeats for 5 times. At the end, the object would move 5 times in axial direction for 1 mm in total, and rotate 60 times for 360° in total.

For each combination of axial parameters, we calculated the coefficients of variation (COV), which is the ratio of the standard deviation to the mean of RMS_P^h or S_P^h over the range of P selected to assess the uniformity of resolution and sensitivity.

E. Phantom Studies

Three phantoms were used to assess the effect of introducing axial movement and the choice of axial sampling parameters on image quality. To focus this study on the spatial sampling issue that affects the systematic error of imaging process, noiseless datasets were used in this study. Other factors that affect the reconstructed images, such as the acquisition time, amount of radioactivity, scatter and attenuation were not considered in this simulation study. The rationale of this approach is that the physics behind spatial sampling and other factors should be independent. With the spatial sampling parameters obtained from this study, the acquisition time of a scan protocol may be determined based on the biological mechanical constraints of the imaging study.

The 1st phantom was composed of 10 pairs of hot and cold orthogonal parallelogram slabs interleaved in the axial direction. The width and thickness (axial) of both slab types are 20 mm and 1 mm, respectively. The voxel size used for the phantom and the reconstructed images was $2 \times 2 \times 0.1 \text{ mm}^3$.

The 2nd phantom is similar but the axial thicknesses of the orthogonal parallelogram slabs increment from one end to the other end of the phantom. The thicknesses of the hot and cold slabs increase from 0.4 mm to 4 mm with a step size of 0.4 mm. The width of all slabs is 20 mm. The voxel size of the reconstructed images was $2 \times 2 \times 0.2 \text{ mm}^3$.

The 3rd phantom consists of hot-rods with different diameters. The sizes of the hot-rods are the same as the well-known

ultra-micro hot-rod phantom (Data Spectrum Inc., Durham, NC). The phantom consists of six sectors, the hot-rods in each sector have same diameter, the center-to-center distance between neighboring rods equals to twice of the rod diameter. The rod diameters in the 6 sectors are 0.75, 1, 1.35, 1.7, 2.0 and 2.4 mm. The reconstructed image voxel size was $0.25 \times 0.25 \times 1 \text{ mm}^3$.

All the phantoms were scanned through an analytical model—obtaining projection data through forward projecting phantom data—with a rotation-only and a helical scan protocol. A set of axial sampling parameters based on non-phantom study result was used for the helical protocol. The system matrix used for virtual scanning and reconstruction was derived from the analytical response function model described in Section II-C. A home-made reconstruction software based on ordered subset expectation maximization (OSEM) algorithm, with 6 subsets was used for image reconstruction. The reconstruction iteration numbers were empirically determined based on the visual inspection of reconstructed images' resolution recovery and severity of artifact. The reconstructed images were evaluated through visual inspection and sectional profile comparison.

III. RESULTS

A. Periodical Pattern of RMS Width

Fig. 4 shows the RMS width of PSF and sensitivity as functions of axial locations over 19.2 mm range. Both functions show periodical patterns with period length of 4.8 mm. The variations of the values are 2 to 3 folds: the sensitivity varies between 0.0092% and 0.0196%, RMS width of PSF varies between 0.22 and 0.73 mm.

B. Evaluation of Axial Movement Sampling Parameters

The clear periodic pattern in Fig. 4 suggests that the helical scan distance L should be multiples of 4.8 mm—the cycle of the periodic pattern, which is the total width of two crystals and the gap between them, as well as that of one periodic cycle of the slats (Fig. 2). This would yield uniform PSFs for any image voxel or object scanned. So we fix L at 4.8 mm in the following reporting. L of other values were tested and, unsurprisingly, showed inferior performance.

Fig. 5 shows the comparison of PSF RMS width and sensitivity between four rotation-plus-axial-movement protocols with different D values. The variations for the rotational scan are much larger than that for any helical scans. Among the scans with different axial step sizes, the variations reduces as the value of D decrease and the uniformity is the best with smallest D value 0.2 mm.

Fig. 6 shows the standard deviations of RMS width and sensitivity over an axial range of 19.2 mm for a series of D values, while L was fixed at 4.8 mm. The value of D varied from 0.05 mm to 0.8 mm with a step size of 0.05 mm—except when L is not a multiple of D . Although the standard deviations continue to decrease at smaller D values, the slope becomes less steep when D is smaller than 0.4 mm. Given that larger step size D is preferred for practical considerations of sampling time each step and the limitation of system matrix size, we

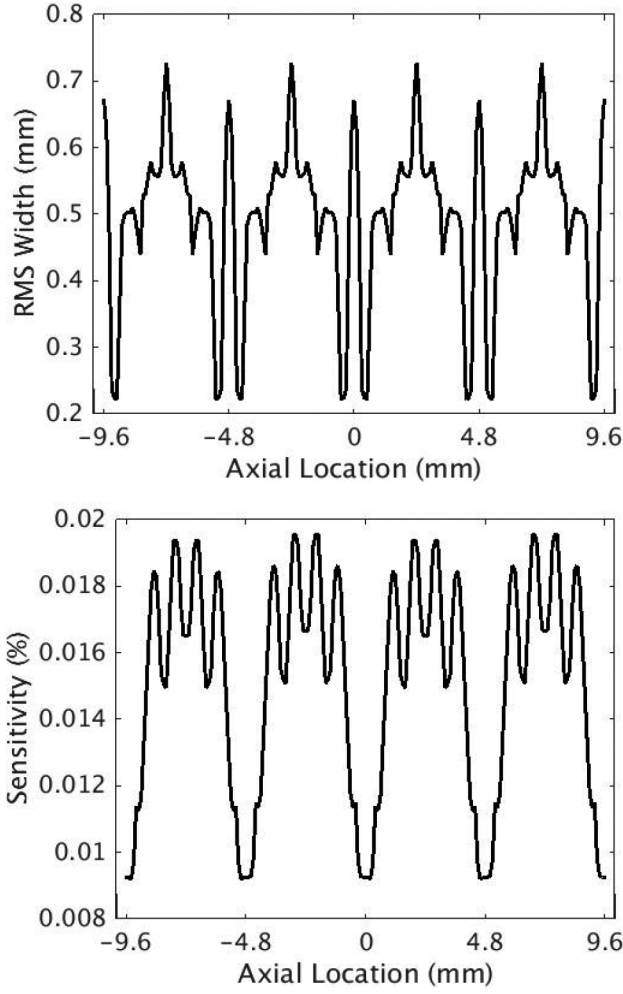
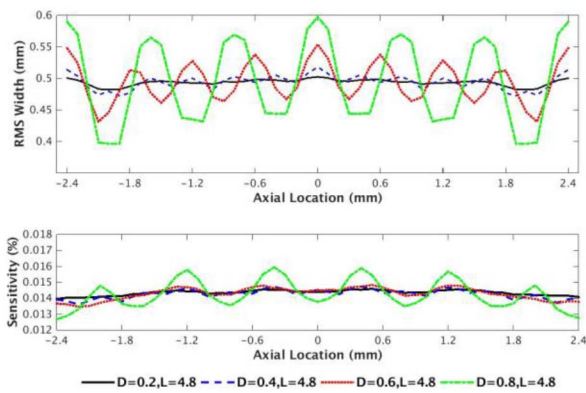


Fig. 4. RMS width of PSF and sensitivity as a function of axial location.

Fig. 5. RMS width and sensitivity as functions of the axial location when L was fixed at 4.8 mm.

select D of 0.2 mm as a representative value for the following helical scan phantom studies.

C. Axial Sampling Parameters on Phantom Studies

Fig. 7 shows the coronal views of the reconstructed images (top) and the section profiles (bottom) of the uniformly-spaced

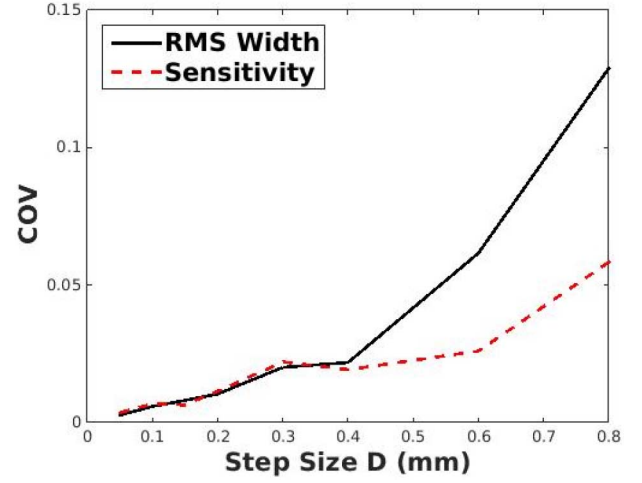
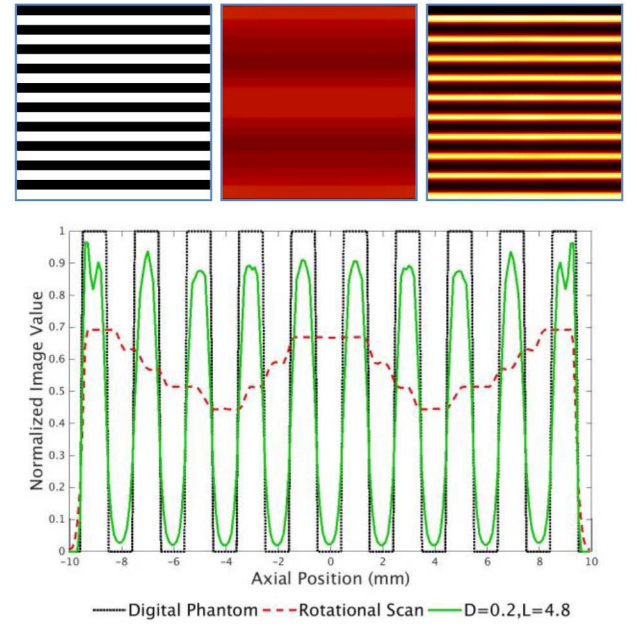
Fig. 6. COV of RMS width and sensitivity with respect to extended D range.

Fig. 7. Coronal images of the digital phantom with equal slab thickness of 1 mm (top-left), scanned with rotation only (top-middle) and helical protocol (top-right), and the axial-direction section profiles (bottom) of the images. The thickness of all slabs (bright color corresponds to hot region) is 1 mm. The iteration number for reconstructing the helical scan was 50.

1-mm thick slab phantom scanned with the rotational and the helical scan ($D = 0.2$ mm, $L = 4.8$ mm). The slabs are not distinguishable in the rotation scan image, but show clear separations in the helical scan image and section profiles, indicating the axial movements improve axial resolution of the SPECT system.

The coronal view images and the images' axial section profiles of the phantom with incremental slab thickness are shown in Fig. 8. The rotational scan can only resolve slabs of 2 mm thick or above. The helical scan, however, resolves slabs of 0.8 mm thick or above. In addition, compared to that of the rotational-scan image, the thicknesses and normalized image values of the slabs in the helical-scan image show superior correlation to that of the original phantom.

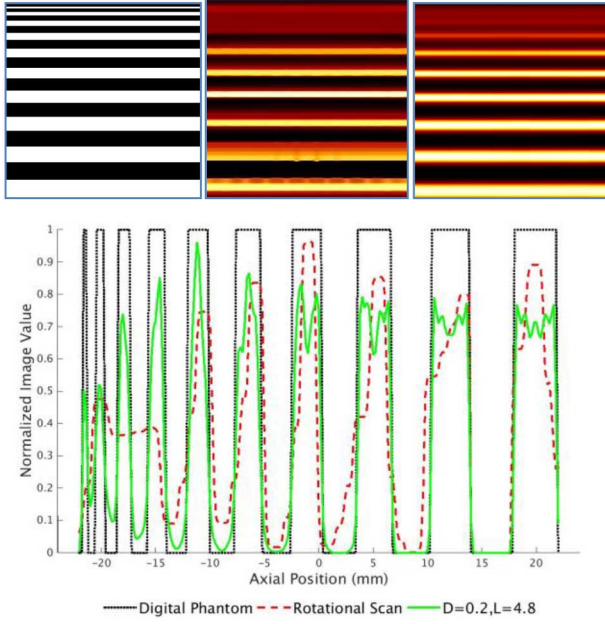


Fig. 8. Coronal images of the digital phantom with incremental slab thickness (top-left), scanned with rotation only (top-middle) and helical scan protocol (top-right), and the axial-direction section profiles (bottom) of the images. The thickness of slabs (bright color corresponds to hot region) increases from 0.4 mm to 4 mm with a step size of 0.4 mm. The iteration number for reconstructing the helical scan was 20.

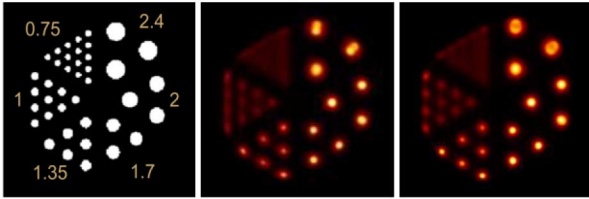


Fig. 9. The transverse view images of the hot-rod phantom in its original form (left), obtained through rotation-only scan (middle) and helical scan (right). The iteration number for reconstructing the helical scan was 50.

Fig. 9 shows the transverse view of ultra-micro hot-rod phantom acquired with the rotation only and helical scans. The 1-mm hot-rod sector at 9 o'clock position is the smallest pattern that is distinguishable in both rotation-only and helical scan images, but the helical scan shows visible clearer separation of the rods. In addition, the two large rods near the top-right corner of the image appear elongated in the radial direction in the middle image but becomes circular in the right image. This indicates helical scan also improves resolution and reduces artifacts in the transverse plane.

IV. DISCUSSION AND CONCLUSION

We have shown that introducing axial movement to the rotational scan protocol, i.e. using helical scan, achieved several improvements to the image quality of the SPECT system. First, helical scan has a clear advantage over the conventional rotational scan in providing more uniform axial system response on the slit-slat SPECT. This confirms the basic concept that the overall effect of sampling an image point at multiple axial locations averages out the variations. Second, the reconstructed-image res-

olution improved in both axial direction and in transverse plane, and the artifacts reduced in the transverse plane.

The improvements to image quality may be explained with the geometrical super-resolution reconstruction theory [11]. In the current SPECT setup, the details of the original image are blurred first by the response function of the slats' opening and then by the under-sampling of the pixelated detectors. By taking multiple images at shifted sub-pixel axial positions, we obtained phase-shift information in the acquired data which can be used to recover the blurring by detector sampling. With slat-opening being the only remaining main blurring factor, the estimated distinguishable width of a bar-pattern (that is collimator resolution) is about 0.84 mm, which matches closely to the observed 0.8 mm distinguishable slat-pattern thickness in Fig. 8. So the helical scan protocol improves the axial resolution to the limit set by the slat collimator geometry. The rotation-only scan protocol, however, does not acquire phase-shift information, therefore unable to take advantage of super-resolution data-acquisition algorithm.

The benefit of super-resolution data-acquisition also extends into the transverse plane. On one end, the helical scan involves taking multiple finer angular projection samples at different axial positions, this fulfills the condition of super-resolution recovery. On the other hand, the reconstruction algorithm we implemented for the SPECT system is in fully 3 dimensional (3-D) mode, that is, the projection and back-projection geometry as well as system response functions are executed in 3-D space, therefore the axial and transverse image properties are intrinsically connected. Effects of changes to a component in image generation process, phase-shifted data here in the axial direction, are naturally propagated into the transverse planes, or vice versa. This has produced the image quality improvement in the transverse plane as shown in the middle and right images of Fig. 9: the hot-rods appear sharper, and show more circular shape which is closer to that in the original image.

Most of the rods in the middle and right images of Fig. 9 appear smaller than the originals in the left image, this is because the rims of the rods show reduced intensity in the reconstructed images due to partial volume effect. However, the rims in the two large rods in the 12 to 2 o'clock section in the right image show elevated intensity—that is, ring artifact - than the central areas of the rods. This phenomenon has been explained by Tong *et al.* [12] - the system matrix used in the point-spread-function (PSF) based reconstruction introduces an amplified frequency band that creates the ring artifact. The artifact depends on the attributes of the system matrix such as condition number (ratio of the largest singular value and the smallest) and consequently the imaging object's characteristics in the corresponding frequency band. Tong *et al.* also showed a band-suppression filter approach that we may use to mitigate the ring artifact.

The periodic pattern of the system response in axial direction, Fig. 4, provides a straightforward answer to the question on choosing the axial movement distance L —the periodic cycle length 4.8 mm. This choice capitalizes the multiple-sample concept of helical scan and leaves only axial step size D to decide.

The choice of D is a balance of achieving imaging performance and satisfying practical constraints. A D value of 0.2 mm was selected for this reason. Figs. 5 and 6 shows that smaller D

provides higher uniformity of axial system response, but using very fine axial step size would raise practical concerns of increased system matrix size and loss of acquisition time due to movement transition overhead—many starts and stops. In each of the phantom studies reported, the voxel size for the reconstructed image was selected first to be adequately small to study the axial or transverse resolution performance the study is designed for, and second to be as large as possible to minimize the system matrix size and therefore save computer storage and computation load. For example, the system matrix size used for the hot-rod phantom was 7.3 GB, it would be 29.2 GB if voxel size is $0.25 \times 0.25 \times 0.25 \text{ mm}^3$ —the scanner consists of 32×192 crystals. The estimate of the acquisition-time loss depends mostly on the mechanical transition time: if the transition time for each mechanical start and stop is 1 second, the hot-rod scan would have a loss of acquisition time of 60 seconds. For a 30 minutes scan, this accounts for about 3% of total acquisition time.

As an informed guess, the choice of L in this study may be extended to being the least common multiples of slat and crystal cycles. By design, the slat and crystal configurations in this study forms a simplified geometrical setup—the cycle lengths of slats and crystals are exactly same. In reality, these two cycles can be different, but the general concept of averaging effect of multiple sampling prevails regardless of the specific cycles of slats or crystals.

REFERENCES

- [1] R. Yao, X. Deng, J. Beaudoin, T. Ma, J. Cadorette, and Z. Cao *et al.*, “Initial evaluation of LabPET/SPECT dual modality animal imaging system,” *IEEE Trans. Nucl. Sci.*, vol. 60, no. 1, pp. 76–81, Feb. 2013.
- [2] S. D. Metzler, R. Accorsi, J. R. Novak, A. S. Ayan, and R. J. Jaszczyk, “On-axis sensitivity and resolution of a slit-slat collimator,” *J. Nucl. Med.*, vol. 47, pp. 1884–1890, 2006.
- [3] Y. Li, J. Oldendick, C. E. Ordonez, and W. Chang, “The geometric response function for convergent slit-slat collimators,” *Phys. Med. Biol.*, vol. 54, p. 1469, 2009.
- [4] W. Rogers, N. Clinthorne, J. Stamos, K. Koral, R. Mayans, and J. Keyes *et al.*, “SPRINT: A stationary detector single photon ring tomograph for brain imaging,” *IEEE Trans. Med. Imag.*, vol. 1, pp. 63–68, 1982.
- [5] R. Accorsi, J. R. Novak, A. S. Ayan, and S. D. Metzler, “Derivation and validation of a sensitivity formula for slit-slat collimation,” *IEEE Trans. Med. Imag.*, vol. 27, pp. 709–722, 2008.
- [6] R. Yao, T. Ma, and Y. Shao, “Derivation of system matrix from simulation data for an animal SPECT with slit-slat collimator,” *IEEE Trans. Nucl. Sci.*, vol. 56, no. 5, pp. 2651–2658, Oct. 2009.
- [7] M. Bergeron, J. Cadorette, J.-F. Beaudoin, M. D. Lepage, G. Robert, and V. Selivanov *et al.*, “Performance evaluation of the LabPET APD-based digital PET scanner,” *IEEE Trans. Nucl. Sci.*, vol. 56, no. 1, pp. 10–16, Feb. 2009.
- [8] X. Deng, T. Ma, R. Lecomte, and R. Yao, “Optimization and calibration of slat position for a SPECT with slit-slat collimator and pixelated detector crystals,” *IEEE Trans. Nucl. Sci.*, vol. 58, no. 5, pp. 2234–2243, Oct. 2011.
- [9] S. D. Metzler, J. E. Bowsher, K. L. Greer, and R. J. Jaszczyk, “Analytic determination of the pinhole collimator’s point-spread function and RMS resolution with penetration,” *IEEE Trans. Med. Imag.*, vol. 21, pp. 878–887, 2002.
- [10] S. Cherry, J. A. Sorenson, and M. E. Phelps, *Physics in Nuclear Medicine*. New York, NY, USA: Elsevier Science Health Science Division, 2012, p. 265.
- [11] J. D. Simpkins and R. L. Stevenson, “An introduction to super-resolution imaging,” in *Mathematical Optics: Classical, Quantum, and Computational Methods*, V. Lakshminarayanan, M. Calvo, and T. Alieva, Eds., ed. Boca Raton, FL, USA: CRC Press, 2012, pp. 539–564.
- [12] S. Tong, A. M. Alessio, K. Thielemans, C. Stearns, S. Ross, and P. E. Kinahan, “Properties and mitigation of edge artifacts in PSF-Based PET reconstruction,” *IEEE Trans. Nucl. Sci.*, vol. 58, no. 5, pp. 2264–2275, Oct. 2011.